Geophys. J. Int. (1999) **139,** 419–432

The crustal structure beneath the northwest fjords, Iceland, from receiver functions and surface waves

Z. J. Du and G. R. Foulger

Department of Geological Sciences, University of Durham, Durham DH1 3LE, *UK. E-mail: z.j.du@durham.ac.uk; g.r.foulger@durham.ac.uk*

Accepted 1999 June 16. Received 1999 June 14; in original form 1999 February 12

SUMMARY

Five broad-band seismic stations were operated in the northwest fjords area of Iceland from 1996 to 1998 as part of the Iceland Hotspot project. The structures of the upper 35 km or so beneath these stations were determined by the modelling and joint inversion of receiver functions and regional surface wave phase velocities. More than 40 teleseismic events and a few regional events containing high-quality surface wave trains were used. Although the middle period passband of the seismograms is corrupted by oceanic microseismic noise, which hinders the interpretation of structural details, the inversions reveal the overall features. Many profiles obtained exhibit large velocity gradients in the upper 5 km or so, smaller zero gradients below this, and, at $\sim$23 km depth, a zone 2–4 km thick with higher velocity gradients. The two shallower intervals are fairly consistent with the 'upper' and 'lower' crust, defined by Flovenz (1980). The deep zone of enhanced velocity gradient seems to correspond to the sharp reflector first reported by Bjarnason *et al.* (1993) and identified by them as the 'Moho'. However, this type of structure is not ubiquitous beneath the northwest fjords area. The distinctiveness of the three intervals is variable, and in some cases a structure with velocity gradient increasing smoothly with depth is observed. We term these two end-members structures of the first and second types respectively. Structures of the second type correlate with older areas. Substantial variation in fundamental structure is to be expected in Iceland because of the great geological heterogeneity there.

Key words: Iceland, joint inversion, modelling, receiver functions, surface waves, velocity gradients.

INTRODUCTION

During the past few decades, seismic refraction data have been intensively used to determine the crustal structure of Iceland. Three main models have been proposed. Among them, the model derived by Gebrande *et al.* (1980) involves a relatively thin ($<$15 km) crust, and the model suggested by Flovenz (1992) involves a thin and almost perfectly molten layer at the crust–mantle transition below a crust 10–15 km thick. The model obtained by Bjarnason *et al.* (1993) has a thicker crust ($>$20 km). More recently, from seismic exploration profiles in northeast Iceland, White *et al.* (1996) determined a crustal thickness reaching 35 km. The nature of the crust and uppermost mantle in Iceland is thus controversial and there has been debate for two decades over whether the crust beneath Iceland is relatively thin ($<$15 km) and hot, or thicker ($>$20 km) and cooler.

One major problem in previous seismic reflection studies was the shortage of direct seismic evidence from the low-velocity-gradient lower crust. Because of the limited bandwidth of the analogue recording system used, which blurred secondary arrivals or detected them only poorly, Gebrande *et al.* (1980) derived a Moho depth based mainly on the V_P/V_S ratio, which they measured from anomalous low-velocity *S* waves travelling at depths greater than 10 km. The value they obtained was 1.96. This ratio was later re-examined by Menke *et al.* (1996), who suggested that Gebrande *et al.* (1980) had misidentified *SmS* as *S* and that the correct value of V_P/V_S shown by these data is $\sim$1.76. Bjarnason *et al.* (1993) found a reflector at a depth of 20–24 km in southwest Iceland from the 170-km SIST (South Iceland Seismic Tomography) profile. Because only a few rays turned at depths greater than 15 km in their seismic profile, the deeper parts of their model were deduced by trial-and-error forward ray-tracing modelling. The lower crustal velocities were not well constrained. Most recently, Darbyshire *et al.* (1998) studied the crust in central Iceland using data from the 310-km long ICEMELT seismic profile. Again, the lower crust was sampled by only a few arrivals from two powerful end shots. Their identified *PmP* phases, wide-angle reflections from the Moho, give a crustal thickness of about 25 km for the north end of the profile, increasing to 38–40 km beneath southern central Iceland.

From 1996 to 1998 a network of 35 broad-band seismometers was operated in Iceland (Fig. 1) as part of the Iceland Hotspot project. The large data set obtained enables the problem of the Icelandic crust to be investigated in an alternative way. Teleseismic *P* waves from epicentral distances greater than 40° pass steeply through the crust, and the first 20–30 s of the waveform contains information about local structure. Receiver function modelling is a powerful means of obtaining shear-velocity profiles of the crust and upper mantle because the timing and amplitude of P_s conversions provide a good constraint on the locations and velocities associated with major crustal and upper mantle discontinuities.

A receiver function contains little absolute velocity information, however. This gives rise to a non-uniqueness problem known as the velocity–depth ambiguity (Ammon *et al.* 1990). Independent constraints on velocity from other *a priori* geophysical sources are required. Most refraction studies of the crustal structure of Iceland have been carried out in the central and eastern part of the island. There have been a few medium-length refraction studies of the northwest fjords area (Bath 1960; Palmason 1971) but there are no published results from deep crustal seismic studies. We address the non-uniqueness problem by combining receiver function inversion with surface wave data. Surface wave phase velocities are sensitive to the average *S*-wave velocity structure of the material in the depth range that the waves penetrate. However, they constrain only weakly the depths to interfaces. Thus, the two methods are complementary.

The data used in this study are broad-band seismograms recorded by five stations HOT06 to HOT10 (Fig. 1), which cover the northwest fjords of Iceland. These stations were equipped with three-component CMG-3ESP seismometers, which have a flat velocity response in the frequency range 0.02 to 30 Hz, and Refraction Technology 72a-02 24-bit data loggers that recorded at 20 samples s^{-1}. Absolute timing was provided by the GPS. The vertical and horizontal sensor components at each station were adjusted to give similar amplitude and phase responses.

DATA

The oceanic location of Iceland means that microseisms dominate the broad-band seismograms. As shown in Fig. 2, seismic signals from moderate earthquakes are obscured. The dominant mechanism for generating microseisms in the frequency range 0.1–5 Hz is non-linear ocean wave interaction (Kibblewhite 1988; Kibblewhite & Wu 1989a,b). We low-pass filter the broad-band seismograms with a corner frequency of 0.1 Hz, which largely removes the microseisms (Fig. 3). However, the dominant frequencies of a teleseismic *P* wave are in the range one to a few seconds, and the wavelength of a shear wave with a frequency of 1 Hz in typical crust is about

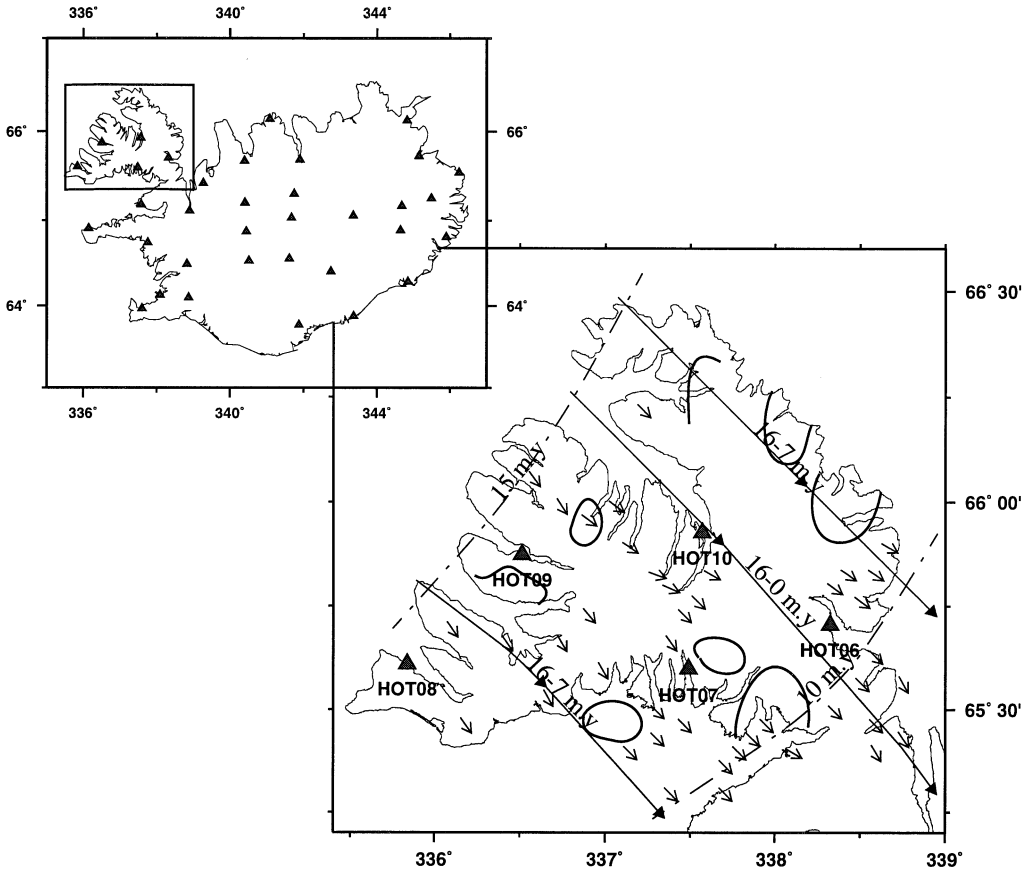

Figure 1. Map of the northwest fjords of Iceland showing locations of the Iceland Hotspot Project stations HOT06–HOT10 and isochrons on land from Saemundsson (1979) and Johannesson & Saemundsson (1998). Bold lines show the outlines of central volcano systems. Arrows show the direction of dip of the lava pile. The inset shows the location of the study area in Iceland.

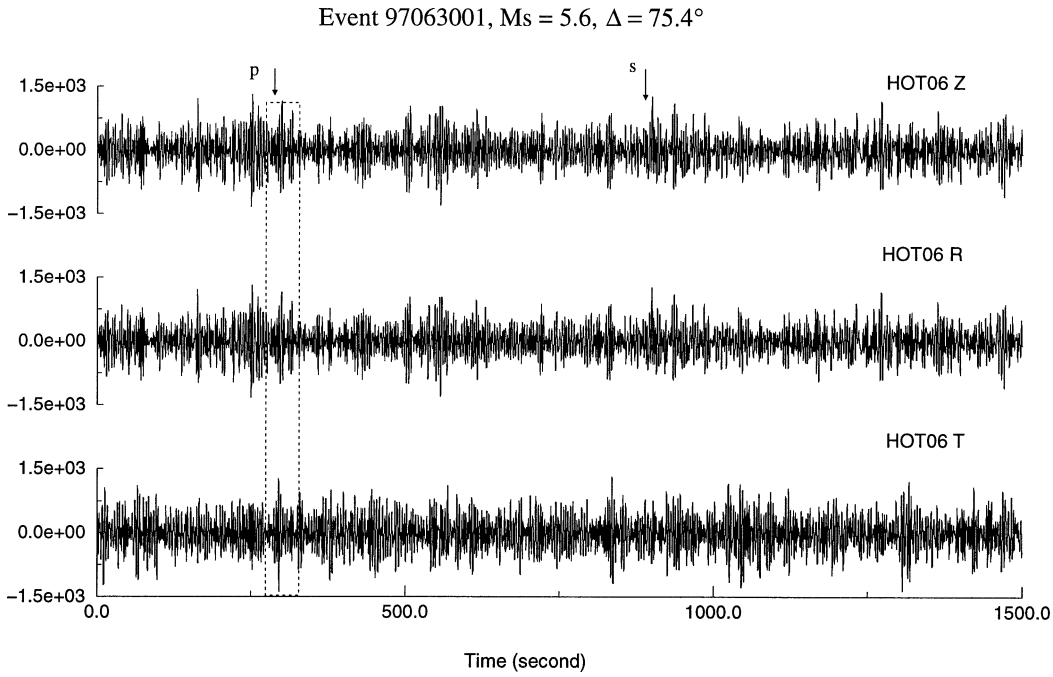

Figure 2. Three-component recordings of event 96063001, which was offshore west of Honshu, Japan, $M_s = 5.6$, recorded at station HOT06. The amplitude is in digital counts. The arrows mark the *P* and *S* arrival times. The time window displayed in Fig. 4 is indicated.

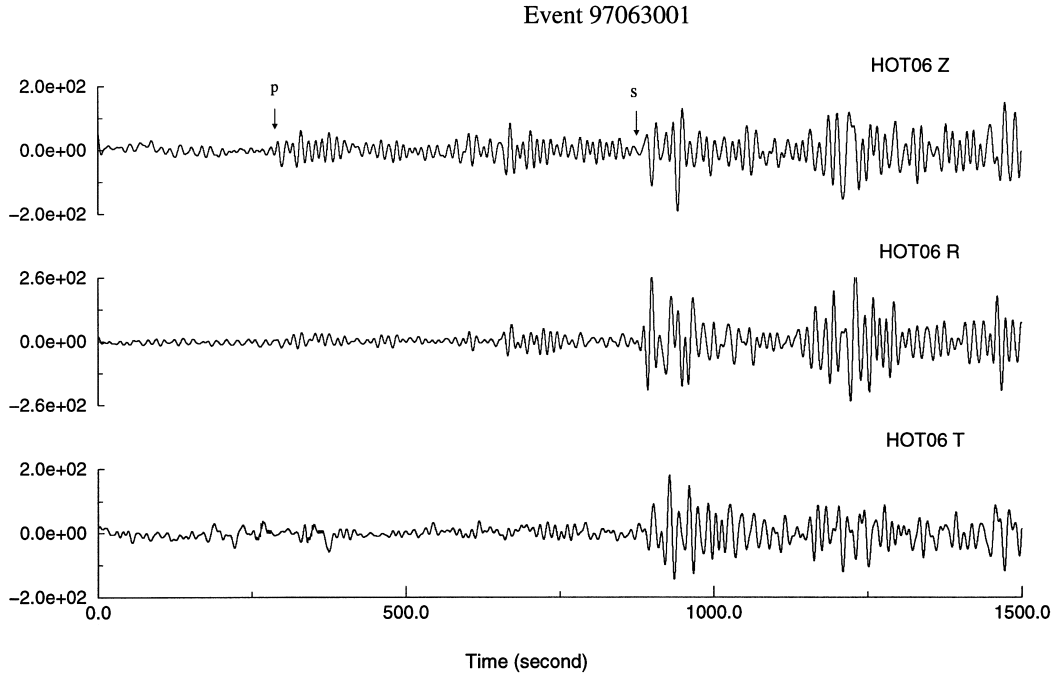

Figure 3. As Fig. 2, but low-pass filtered at 0.1 Hz.

4 km. The sensitivity of the inverse modelling depends on the frequency content of the receiver functions, and structural models consisting of layers as thin as 1 km can only be resolved if the receiver function contains frequencies as high as 1 s. In the case of the Icelandic data, we thus need to find a way to retrieve power from the contaminated seismograms, so that the useful signal bandwidth is broadened from 10 s to one or a few seconds.

Receiver functions

We investigate the abilities of the source-equalization procedure of frequency domain receiver function analysis (Langston 1979), which is used to produce the radial and tangential receiver functions, and also to remove source and propagation path effects. Fig. 4 shows an example of deconvolution of the vertical component seismogram from both radial and tangential

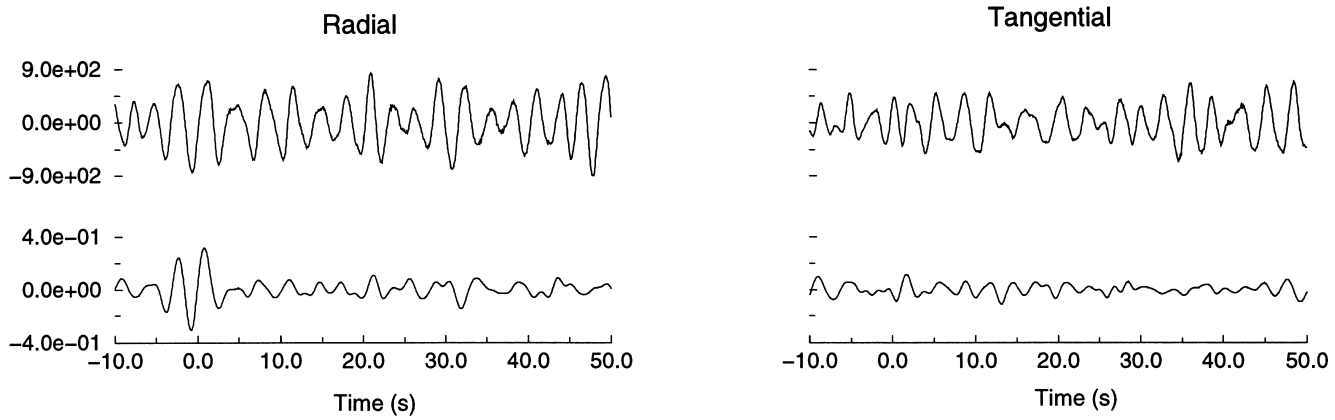

Figure 4. Top traces: original seismograms. Lower traces: radial and tangential receiver functions, computed from the seismograms shown in Fig. 2. The *P* arrival can be seen at time zero on the radial receiver function.

seismograms for the recordings shown in Fig. 2. This procedure also suppresses oceanic noise because contamination of the wave trains by ocean interaction can be regarded as an additional path effect (compare Figs 2 and 4). This is despite the fact that the frequency content of the teleseisms is dependent on event magnitude and epicentral distance, whereas microseisms have a dominant spectral band with a lower frequency corner above 0.1 Hz. We used a Gaussian low-pass filter with a corner frequency of 1.2 Hz to remove high-frequency noise. Most events with magnitudes greater than $M_s = 5.6$ and epicentral distances greater than about 50° were useful for our receiver function analysis, since the deconvolution procedure clearly suppressed the oceanic noise. There were a few exceptions where this was not successful, and in our analysis we excluded these exceptional events.

We selected more than 40 teleseismic events that cluster in three backazimuths: southwest (backazimuths of $\alpha = 238°$ to 263° and epicentral distances from $\Delta = 59°$ to 85°); northeast ($\alpha = 53°$ to 75° and $\Delta = 57°$ to 81°); and north ($\alpha = 8°$ to 29° and $\Delta = 60°$ to 84°). The deconvolution was carried out using a spectral trough filler, c, around 0.01–0.001, by considering the form of the averaging functions (the vertical component deconvolved from itself, with given c values).

Stacking receiver functions were used here to mitigate further noise in the data. Since receiver functions corresponding to events from different distances have large amplitude differences, which may lead to an inaccurate composite waveform, we scaled the receiver functions to unit amplitude prior to stacking. As an example of our data, we show the whole set of radial and tangential receiver functions and their stacking for station HOT08 (Fig. 5). Although the wave shape details from similar backazimuths are diverse, similarities of the waveforms from different events can also be seen. Note the high pre-signal noise, before the *P* wave, at the beginning of each stacked trace and the large amplitudes of the tangential receiver functions, indicating that the signal-to-noise ratio remains low after the stacking. The large amplitudes of the tangential receiver functions may also be due to wave scattering, and the existence of dipping structure or medium anisotropy underneath the stations. There are significant waveform differences among the three backazimuths due to structural backazimuthal variations.

In Fig. 6, the stacked radial receiver functions for the five stations and different backazimuths are shown. There are no data for station HOT09 from the northeast. Although the distance between stations is small, we can see clear waveform pattern changes from station to station and from backazimuth to backazimuth. The only observable common feature is the P_s converted phase, which arrives about 3.0 s after the *P* wave. This phase is clear on most of the traces from the southwest backazimuth, it is visible but of low amplitude on the traces from the northeast backazimuth, and is essentially absent on the traces from the north backazimuth. Secondary reverberations are visible but are not coherent from station to station for each backazimuth, and no coherent multiples can be seen on any of the stacked waveforms.

Surface waves

We select only those high-quality regional events with interstation ray paths (Fig. 7), since we want to measure the dispersion between station pairs. We analyse data using the FTAN (frequency–time domain analysis) package (Levshin *et al.* 1992). Unfortunately, all surface wave measurements currently depend crucially on direct human interaction with seismic waveforms. Accurately identifying the main dispersion ridge, separating the 'direct arrival' from the surface wave coda at periods below 25 s, and truncating the measurements appropriately at long periods as the signals weaken, involve many uncertainties (Fig. 8). For this reason, instead of measuring the phase velocities from a single event, we compute an average dispersion curve from several events with a correlation coefficient of 0.97 or higher (Fig. 9) for each station pair. The computed average phase velocity dispersion curves are shown in Fig. 10 for the three station pairs HOT08–HOT09, HOT10–HOT07 and HOT09–HOT07. There were insufficient data to measure the dispersion between stations HOT10 and HOT06. The events used for the path HOT08–HOT09 were within a range of 1000 km, so we were able to go down to periods as short as 7 s. For the other two paths we could only measure the dispersion for periods greater than 10 s since the events were 2500–3000 km away.

THE JOINT INVERSION

We adopt the receiver function inversion method of Ammon *et al.* (1990). We extend the method to allow simultaneous inversion of the receiver function waveform and the measured

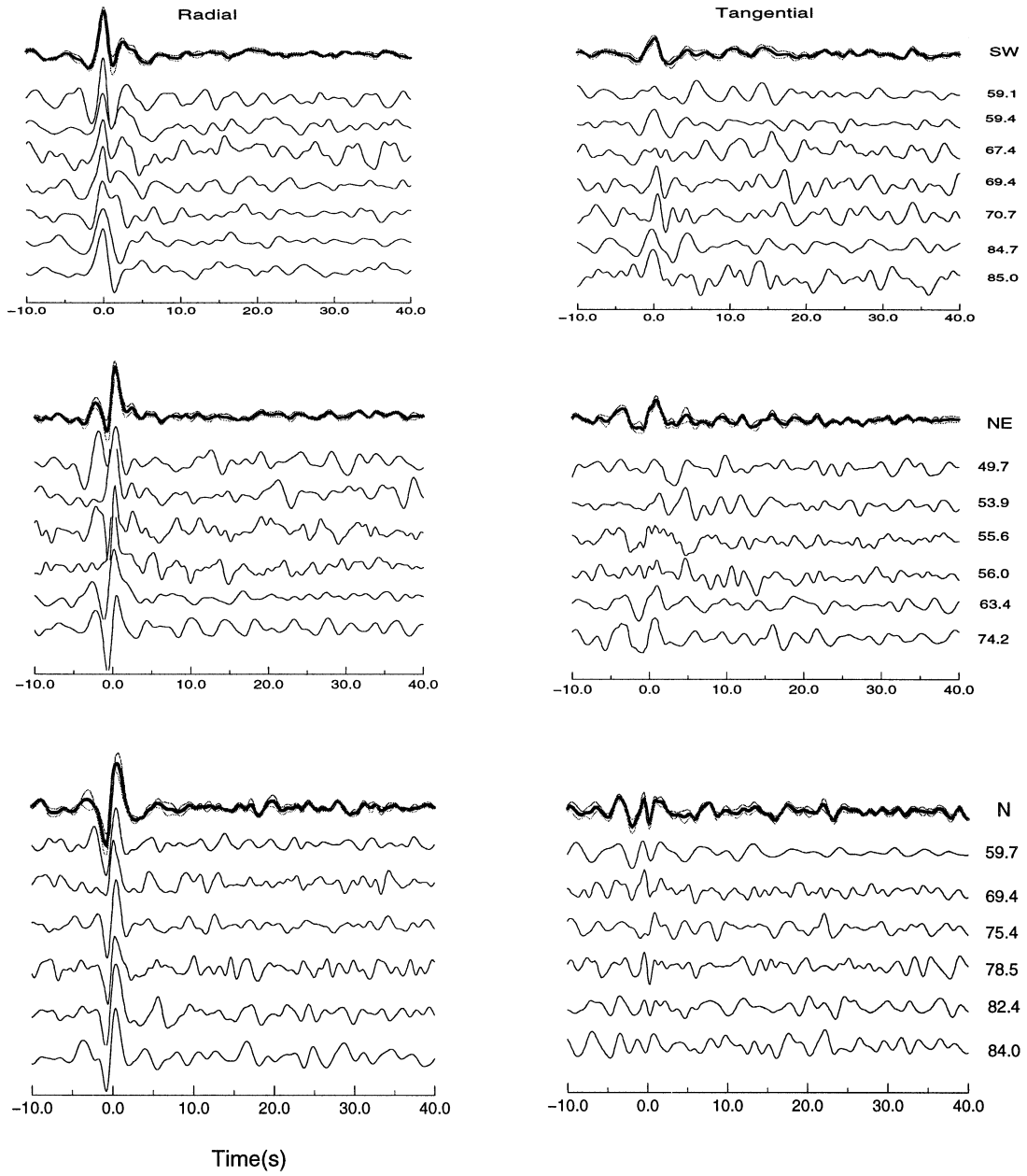

Figure 5. Stacking receiver functions for three backazimuths (top: southwest; middle: northeast; bottom: north), for station HOT08. For the top trace in each panel, the thick line is the stacked receiver function and the dotted lines around it indicate one standard deviation. The numbers in the right-hand column give epicentral distances in degrees.

surface wave dispersion curve. The use of more surface wave data, rather than using only a pair of periods (Ozalaybey *et al.* 1997), provides additional model constraints because different periods sample different regions of the model space. The final solution is sought by fitting both the receiver function waveforms and the phase velocity dispersion curves.

The system equations are

$$\begin{bmatrix} \mathbf{D} \\ \mathbf{C} \\ \sigma\mathbf{\Delta} \end{bmatrix} \mathbf{m} \approx \begin{bmatrix} \mathbf{r} \\ \mathbf{c} \\ \mathbf{0} \end{bmatrix} + \begin{bmatrix} \mathbf{D}\mathbf{m}_0 \\ \mathbf{C}\mathbf{m}_0 \\ \mathbf{0} \end{bmatrix}, \tag{1}$$

where the 'jumping' smooth matrix $\mathbf{\Delta}$ constructs the second difference of the model $\mathbf{m}$ (Constable *et al.* 1987; Ammon *et al.* 1990).

$$\Delta = \begin{bmatrix} 1 & -2 & 1 & 0 & \ldots \\ 0 & 1 & -2 & 1 & \ldots \\ 0 & 0 & 1 & -2 & \ldots \\ 0 & 0 & 0 & 1 & \ldots \\ . & . & . & . & \ldots \end{bmatrix}, \tag{2}$$

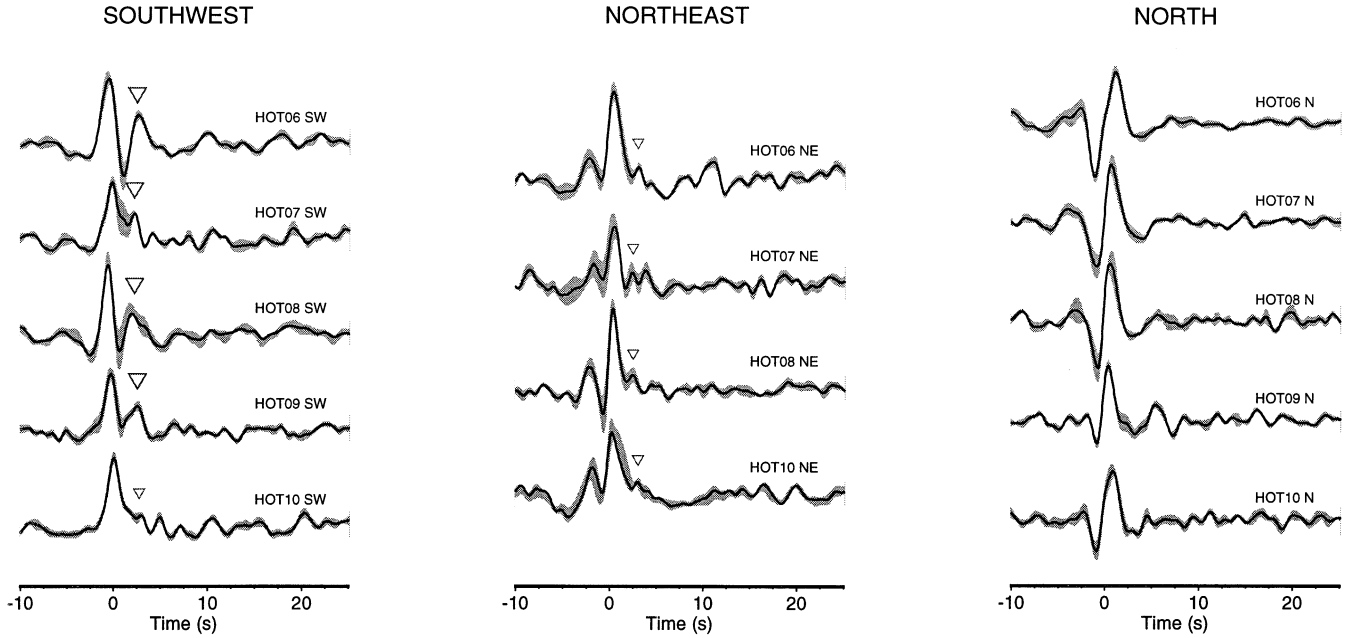

Figure 6. Stacked radial receiver functions for the three backazimuths for all the stations. The shaded regions represent one standard deviation bounds. The inverted triangles indicate the P_s converted phase from reflectors at about 25 km depth.

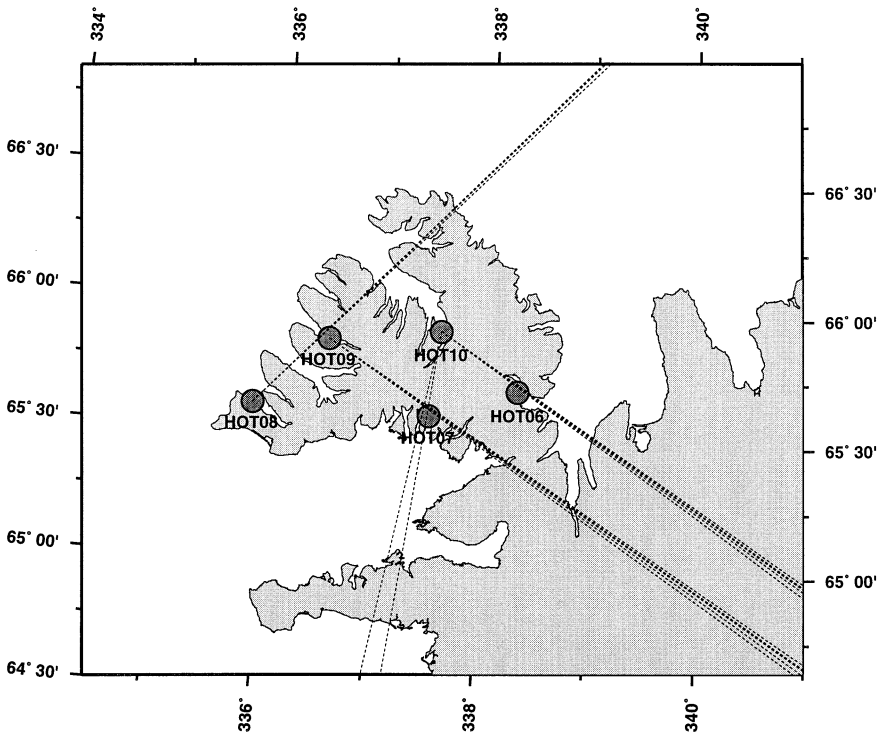

Figure 7. Ray paths of the regional events used to measure Rayleigh wave phase velocities.

where in eq. (1) **D** and **C** are matrices containing, respectively, the partial derivatives of the receiver function and surface wave phase velocity with respect to the velocity model **m**. $\mathbf{m}_0$ is the initial velocity model, σ is the adjustable parameter controlling the trade-off between the waveform and the smoothness of the model (Ammon *et al.* 1990), and **r** and **c** are vectors containing the receiver function waveform and the phase velocity residuals. The Rayleigh wave partial derivatives of phase velocity with respect to the model parameters and the theoretical dispersion curve for a given velocity model are computed with the algorithm described by Du *et al.* (1998).

Using eq. (1), we determine the crustal velocity structure beneath each station, adopting a layered structural model. The *S*-wave velocity is the free parameter in our inversion.

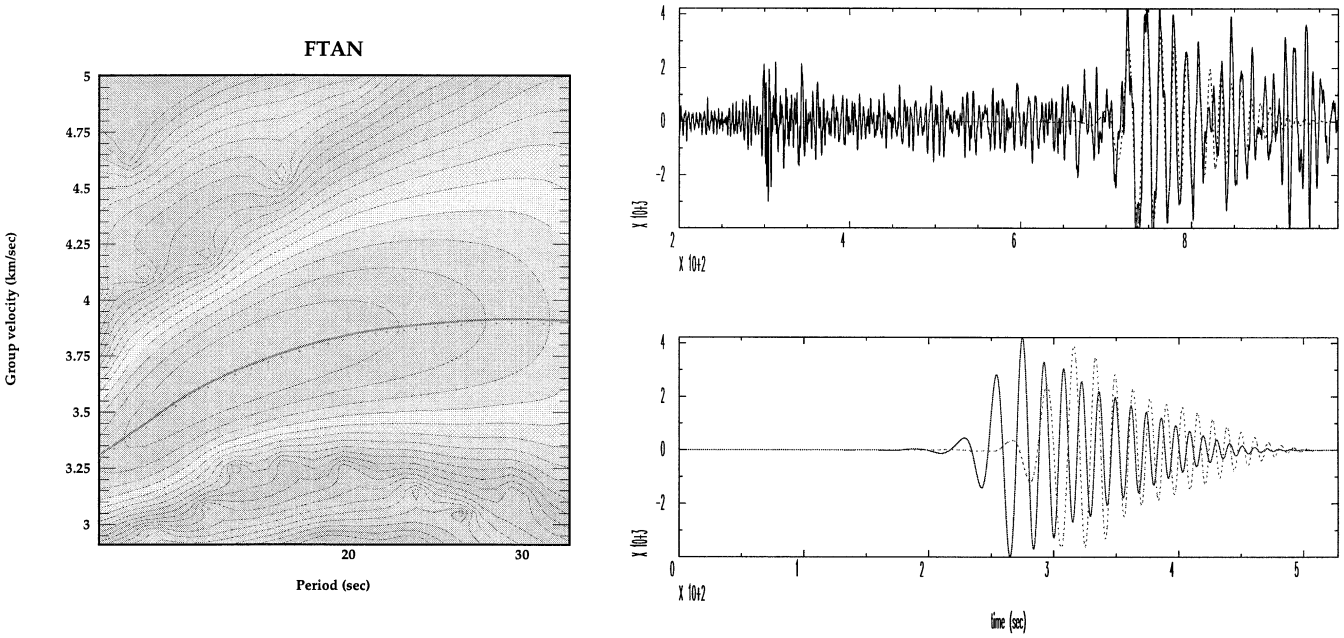

Figure 8. Example of a frequency–time analysis (FTAN) for the vertical component recorded at station HOT07 for an event in the Azores Islands (1997 June 27, $M_s = 5.6$, $\delta = 26°$). The analyst-defined filter removes potentially interfering signals such as body waves, other surface waves and coda. Left: the group velocity curve (solid line) is first picked by hand and this initial estimate is used for automatic refinement on the filtered images. Grey shading indicates energy. Right: top, comparison of the raw (solid line) with the filtered (dashed line) waveforms reveals the effects of the filtering displayed; bottom, filtered waveforms for the recordings at stations HOT07 (solid line) and HOT10 (dashed line), used to estimate the interstation differential phase velocity.

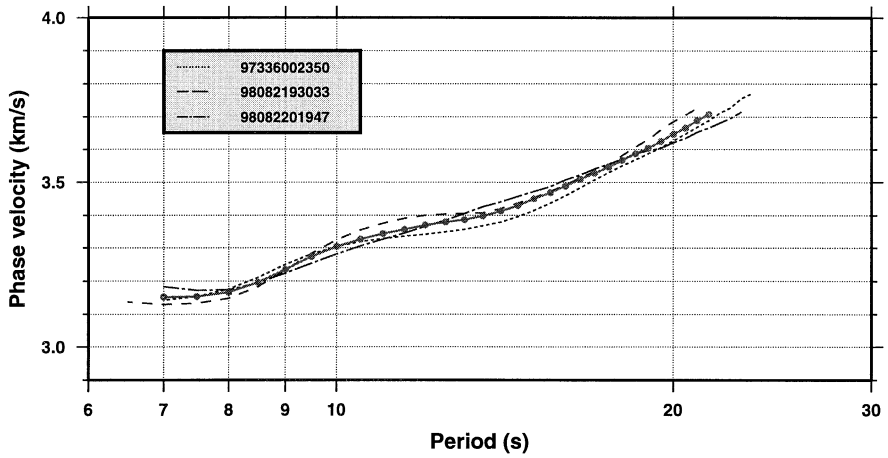

Figure 9. Calculation of the Rayleigh wave average phase velocity dispersion curve for path HOT08–HOT09, from events 97336002350 ($M_s = 5.2$, $\delta = 9°$), 98082193033 ($M_s = 5.3$, $\delta = 8°$) and 98082201947 ($M_s = 5.2$, $\delta = 8°$) all in the Jan Mayen region. The solid thick grey line is the calculated average curve.

The *P*-wave velocity is set assuming a Poisson's ratio of 0.25, and the density is set using the relationship $\rho = 0.32V_P + 0.77$ (Berteussen 1977).

Initial model

To start the inversion, we need an initial model. The joint inversion (eq. 1) adopts a local linearization of the misfit function, which requires an initial model not far from the 'real' crustal structure. If good structural information is available *a priori*, for example deep refraction data, this could conceivably be used to erect an initial model. However, there is only a little information available, and that from several old, short, refraction profiles (Bath 1960; Palmason 1971). There are no published results for deep crustal structure in the region. Here, we adopt an alternative method, involving genetic algorithm searching (Lomax & Snieder 1995), to select our initial models.

We start from a simple trial model (left panels of Figs 11a, 12a and 13a) which is based on the thin-crust model (Gebrande *et al.* 1980; Flovenz & Gunnarsson 1991) at shallow depth (< 15 km), with arbitrary velocity discontinuities added at 5, 15 and 35 km depth to explore the effect of extreme errors in

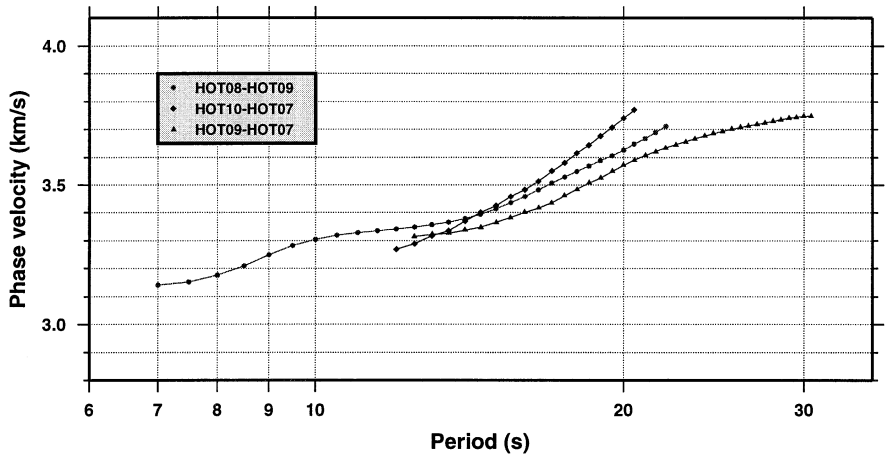

Figure 10. The average Rayleigh wave phase velocity dispersion curves for the interstation ray paths shown in Fig. 7.

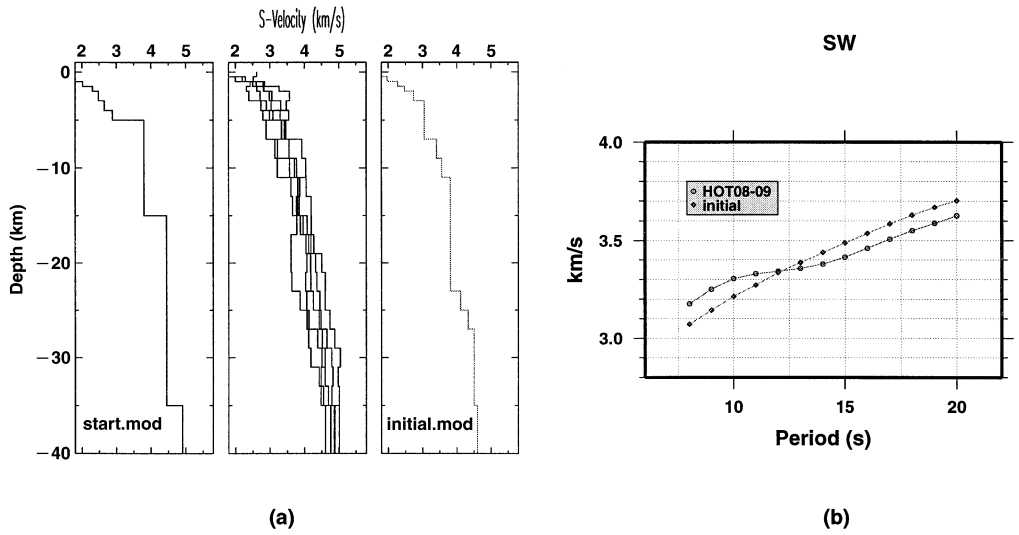

Figure 11. Construction of the initial model for the southwest backazimuth inversion. (a) *S*-wave velocity models: right, initial starting model; middle, smoothest models obtained from many inversions using different weightings (see text for explanation); left, initial model used. (b) Phase velocity dispersion curves measured (small circles) and computed from the initial model (small diamonds).

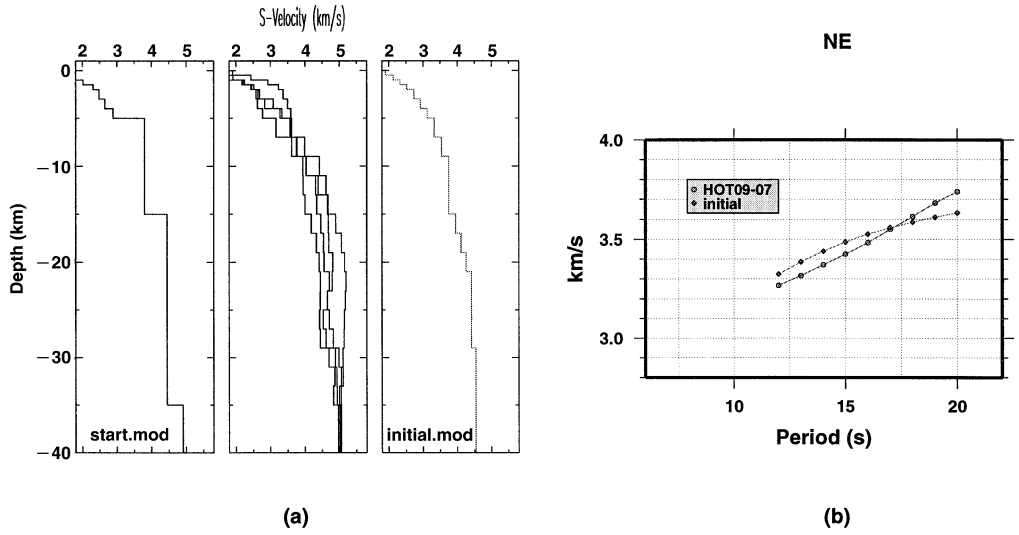

Figure 12. As Fig. 11, but for the northeast backazimuth.

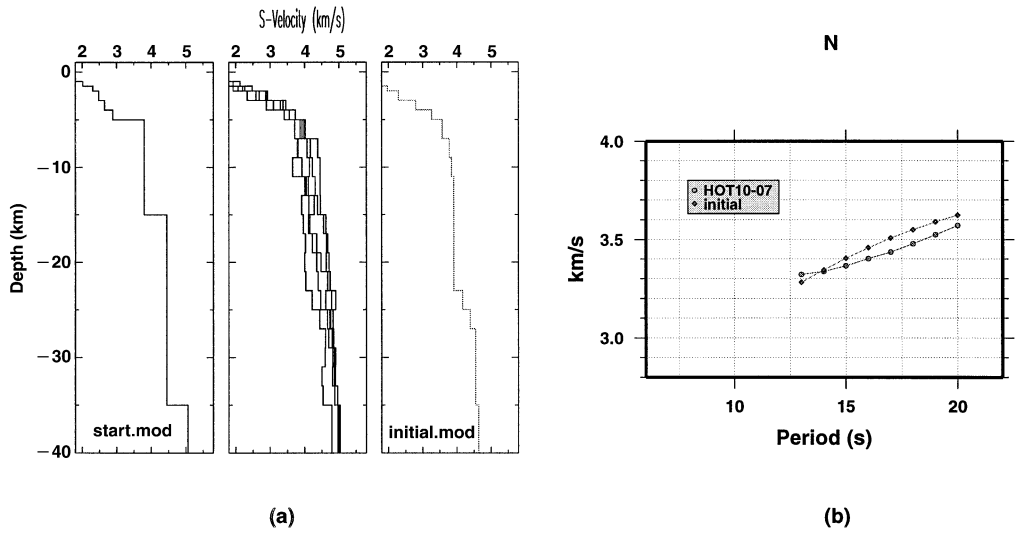

Figure 13. As Fig. 11, but for the north backazimuth.

the starting model. We parametrize this starting model with very thin layers, 0.5 to 1.0 km thick for the first 5 km, and 2.0 to 2.5 km thick for deeper layers. A half-space is placed below a depth of about 40 km.

The preliminary inversion consists of two steps. For each backazimuth, by minimizing the differences between the stacked receiver function and the synthetics computed from the starting model, we first, station by station, perform a single waveform inversion for all the waveforms shown in Fig. 6 using the method of Ammon *et al.* (1990). To test the dependence of the inversion of the starting model, models with broad variations throughout the entire depth range were tried. We constructed models with a maximum cubic perturbation of 0.75 km s^{-1} (maximum cubic vector amplitude), and a maximum random perturbation of 0.15 km s^{-1} (shear velocity distribution variance), after the fashion of Ammon *et al.* (1990), with the genetic searching method (Lomax & Snieder 1995). This amounted to testing over 75 trial initial models for each station. We found that almost all the inversions do not favour velocity jumps at shallow depth, and eliminated the two shallow, sharp discontinuities at depths of 5 and 15 km in the starting model after only two or three iterations. The inversions converged very quickly to the models without these discontinuities.

In the second step, we conduct a suite of inversions with a varying, smooth weighting, using the same number of iterations and solution roughness parameters as obtained in the first step. After these two steps we take the smoothest models (middle panels of Figs 11a, 12a and 13a). Although these models contain no absolute velocity information, they reflect well the locations of major velocity contrasts at crustal discontinuities.

We simplify the smoothest models by keeping only their main features. Although the simplification smears out many model details, their primary sensitivities, which depend on the depth–velocity products and not simple velocities, remain. To constrain further the absolute velocities, we test the simplified models against the surface wave phase velocity dispersion data (Fig. 10). For the southwest backazimuth, we use the data from path HOT08–HOT09, and for the north backazimuth the data from path HOT10–HOT07. The data differences between paths HOT08–HOT09 and HOT09–HOT07 are close to a parallel shift for periods below 20 s (Fig. 10), which indicates that the difference in average medium properties in the crust along these two, almost perpendicular, backazimuths is small. The receiver functions from the northeast backazimuth are broadly similar to those from the southwest (Fig. 6). These two factors strongly support the broad regional structure of the area shown by surface geological observations, which report southeasterly-dipping lava layers (Kristjansson & Johannesson 1996). Since we have no data from the northeast backazimuth, we use the surface wave data from the path HOT09–HOT07. It is appropriate to select surface wave data on the basis of regional azimuthal trends.

For each backazimuth, we thus obtained an optimal model (right panels of Figs 11a, 12a and 13a), which matches the dispersion curve best. The misfits were around ± 0.1 km s^{-1} (Figs 11b, 12b and 13b). These three optimal models serve as our initial models in subsequent inversions.

The southwest backazimuth

In the receiver functions stacked for the southwest backazimuth (Fig. 6), the 3 s, P_s converted phase is most clearly visible. From this backazimuth, we also have a very high-quality surface wave phase velocity dispersion curve (small circles, Fig. 10). Using eq. (1), we perform a joint inversion of the receiver function and the surface wave phase velocity data, starting from the derived initial model (right panel of Fig. 11a). The final velocity models (Fig. 14) fit both the receiver function waveforms and the measured phase velocity curves well. The final velocity models for the northeast and north backazimuths are shown in Figs 15 and 16 and described in subsequent sections.

At station HOT06, the final model predicted waveform lies within the one standard deviation data bounds (shaded) for almost all of the P_s conversion that follows the P arrival (upper panel of Fig. 17). The fit to the data multiples is poorer. The fit to the phase velocity curve is excellent. The differences between the curve predicted from the initial model and the data (see Fig. 11b) have been significantly reduced by the iterative inversion procedure.

The joint inversion eliminates many solutions that would otherwise be obtained from inversion of the receiver function

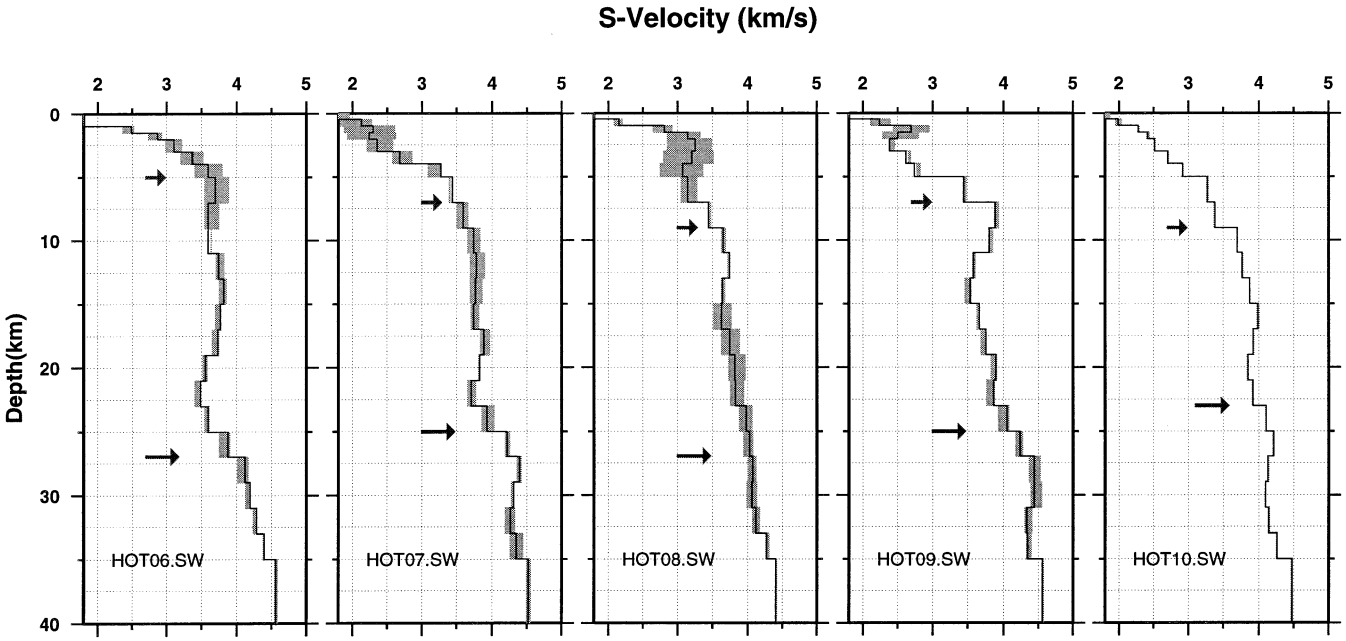

Figure 14. Southwest backazimuth inversion results. The shaded regions define the model uncertainties corresponding to the one standard deviation bounds of the stacked receiver functions. The upper and lower arrows indicate where the velocity exceeds 3.7 km s^{-1} and 4.1 km s^{-1} respectively. These are the average velocities found for the base of the upper and lower crust from refraction data throughout Iceland.

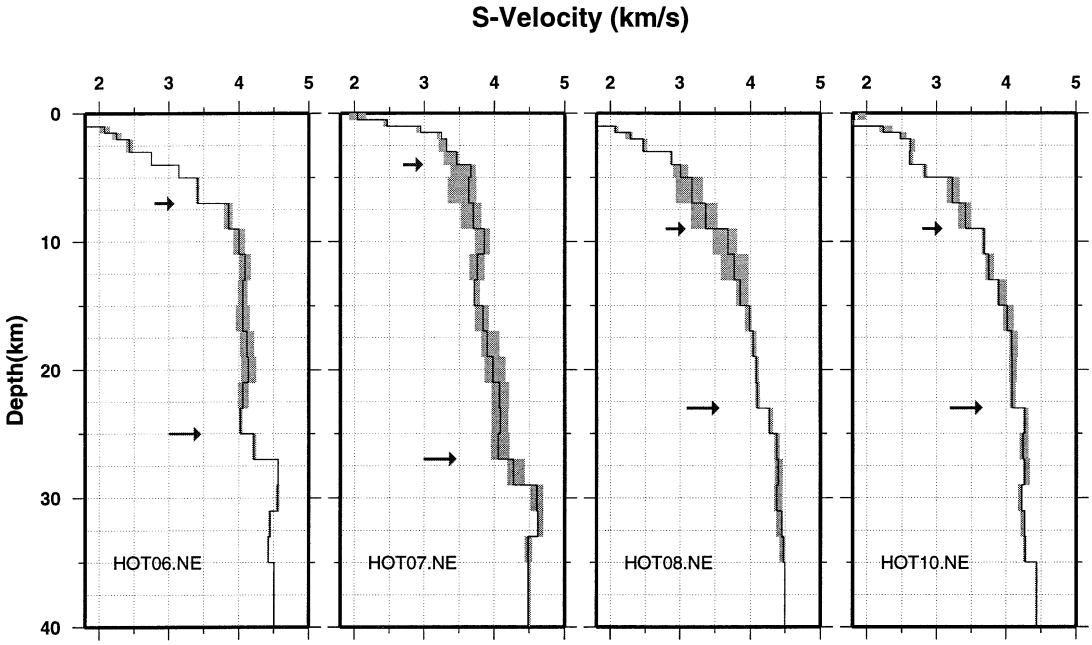

Figure 15. As Fig. 14, but for northeast backazimuth.

alone. The final velocity model uncertainties corresponding to the one standard deviation bounds of the receiver functions are plotted as shaded regions for each model in Figs 14–16. The inversion at station HOT10 is very stable and gives the smallest model uncertainties. As mentioned earlier, the receiver functions resolve velocity discontinuities, and the surface waves resolve average velocities. We positively or negatively perturb the average phase velocity dispersion curve by ± 0.1 km s^{-1} and repeat the inversions (Ozalaybey *et al.* 1997). This results only in changes of much less than ± 0.1 km s^{-1} around the final mean models, with insignificant changes in the main model features.

We summarize our results by comparing them with the main results from recent, long seismic refraction profiles elsewhere in Iceland. We refer to the 'upper' and 'lower' crust using the average velocity values obtained by the SIST and ICEMELT profiles (Bjarnason *et al.* 1993; Darbyshire *et al.* 1998). In Figs 14–16, the depths at which the velocities first exceed 3.7 and 4.1 km s^{-1}, corresponding to the bases of the upper and the lower crust defined by the reflection data, are shown by arrows.

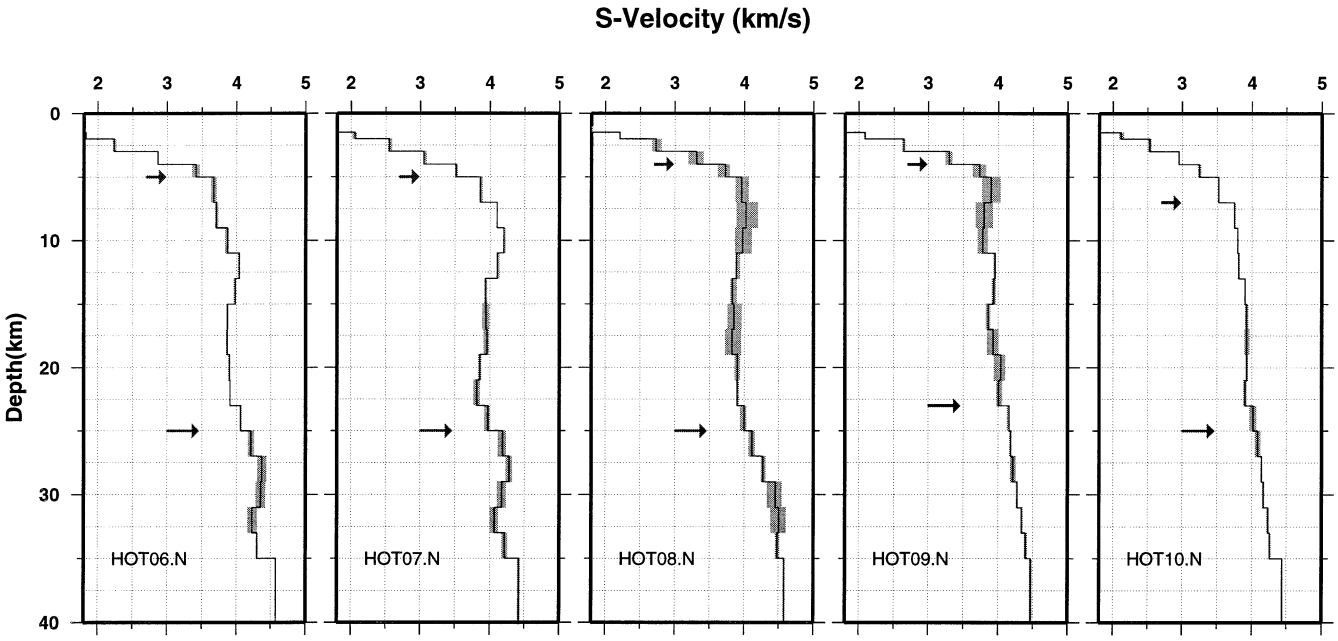

Figure 16. As Fig. 15, but for north backazimuth.

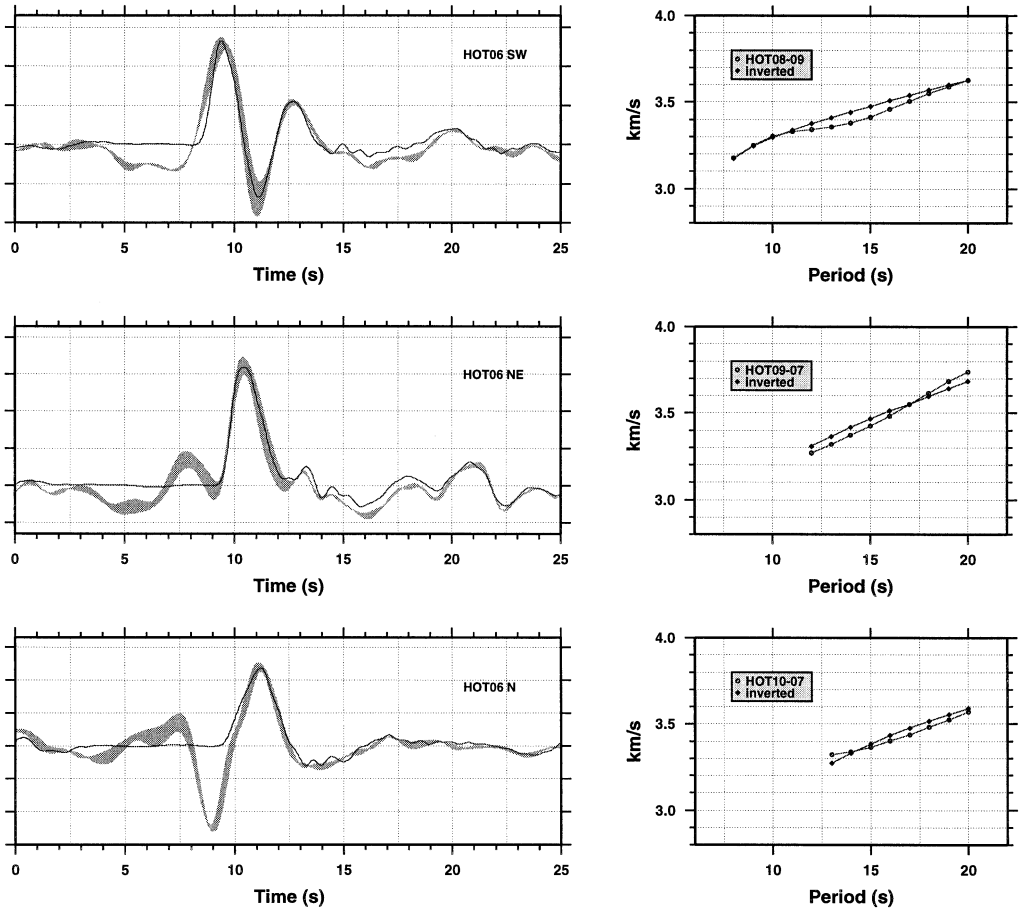

Figure 17. Example of the final fitting of the receiver function waveforms (solid lines are the synthetics computed from the final mean model, shown by solid lines in Figs 14, 15 and 16) and surface wave phase velocity curves, for station HOT06.

Common features of the velocity models are large velocity gradients at shallow depths (0–5 km), decreasing below this in the depth range 8–20 km. There is a systematic increase in velocity gradient that gives rise to the 3 s P_s conversion beneath ~23 km depth under stations HOT06, HOT07 and HOT09. This feature is poorly developed beneath stations HOT08 and HOT10. There are significant structural differences between stations, and variations of one standard deviation in the data

can cause large variations in shallow structure. A high-velocity body at 7–12 km depth is resolved beneath station HOT09. This may be related to an exposed central volcano, located southwest of this station, 15 km along the ray paths (Fig. 1).

The northeast backazimuth

For the northeast backazimuth, we have data for only four stations (Fig. 6). The joint inversion results from the receiver functions and the surface wave data, measured from the interstation path HOT09–HOT07 (small triangles, Fig. 10), are shown in Fig. 15. The middle panel of Fig. 17 gives one data example of the final fit obtained at station HOT06. The initial model for this inversion is shown in Fig. 12a (right panel).

At a depth of 25–27 km, relatively large velocity discontinuities are obtained beneath stations HOT06 and HOT07. This feature is not clear beneath stations HOT08 and HOT10, however, but instead these stations are characterized by a gradational velocity increase at all depths. In the depth range $\sim$10 to 20 km, station HOT06 has an almost constant velocity of about 4.1 km s^{-1}. Except at station HOT07, all stations display a high velocity gradient in the depth range 0–10 km. Station HOT07 is located at the southwest edge of an exposed central volcano (Fig. 1), and the shallow interval beneath it is thin, extending only to 4 km depth. Below this the velocity is high, about 3.7 km s^{-1}, and there is an almost constant, small, positive, velocity gradient to a depth of 27 km.

The north backazimuth

The data quality for the north backazimuth is not good, compared with that for the other backazimuths. The joint inversion results from the receiver functions (Fig. 6) and the surface wave data, measured from the interstation path HOT10–HOT07 (small diamonds, Fig. 10), are shown in Fig. 16. One data example from station HOT06 is shown in the lower panel of Fig. 17. The initial model for the inversions is shown in Fig. 13a (right panel).

A common model feature is the steep velocity gradient in the upper 5 km or so. Beneath this, the velocity is fairly constant at about 4.0 km s^{-1}. Velocity gradients increase again at 23–25 km depth beneath all stations. This increase is large and clear beneath stations HOT06, HOT07 and HOT08, but small and unclear beneath stations HOT09 and HOT10.

DISCUSSION AND CONCLUSIONS

We present here the first results constraining the regional structure of the whole crust beneath the northwest fjords of Iceland. Although there is considerable variation among stations and backazimuths, the first-order crustal features are nevertheless revealed.

The majority of the models obtained from the joint inversion (Figs 14–16) reveal the following features, comprising structures which we term the first type.

(1) The shallowest levels are characterized by high velocity gradients (up to $\sim$0.8 s^{-1}) and this interval is typically $\sim$5 km thick, exceptionally approaching 8 km. *S*-wave velocities at its base are in the range 3.6–4.0 km s^{-1}, corresponding to *P*-wave velocities of 6.34–7.04 km s^{-1}, assuming $V_P/V_S = 1.76$ (Menke *et al.* 1996).

(2) Below the region of high velocity gradients is an interval characterized by an almost constant velocity, or low velocity gradients not exceeding $\sim$0.02 s^{-1}. This interval extends down to 23–27 km depth, at which depth the *S*-wave velocity is typically about 4.1 km s^{-1} (corresponding to a *P*-wave velocity of 7.09 km s^{-1}).

(3) Below the interval of almost constant velocity, the velocity gradient increases again and is as high as 0.20 s^{-1} throughout a depth interval typically 2–5 km thick. The clarity of this feature is variable; for example, beneath stations HOT09 and HOT10 it is poorly developed on the north backazimuth models, where much gentler velocity gradients are obtained, over much larger depth intervals. At its base the *S*-wave velocity is typically 4.4–4.5 km s^{-1} (corresponding to a *P*-wave velocity of 7.71–7.78 km s^{-1}).

A few models display a much smoother velocity–depth profile, notably those determined for the northeast backazimuth for stations HOT08 and HOT10 and for the southwest backazimuth for station HOT10. We term this kind of model a structure of the second type. In these models, the division between the upper crust with high velocity gradients and the lower crust with almost constant velocity is not clear, and neither is a well-defined increase in velocity gradient at depths greater than 20 km. Instead, to first order, the velocity gradient decreases smoothly with depth.

There is considerable backazimuthal variation in the detailed structure obtained, which may be caused by several factors. The receiver function is sensitive to structure on the epicentral side of the station, where reverberations occur as the incoming seismic waves rise up at an angle as they approach the station. Thus seismic waves from different backazimuths and incidence angles sample different volumes around the station. The surface wave dispersion curves (Fig. 10) show clear variations in average medium properties at periods of 12–20 s between the north and other two backazimuths. The P_s converted phase, about 3.0 s after *P*, is also absent from the north backazimuth receiver functions (Fig. 6). This backazimuthal variation agrees with geological observations that surface lava layers dip to the southeast in this region (Kristjansson & Johannesson 1996). This feature could be studied in some detail in the future, by modelling the tangential receiver functions, if effective noise reduction methods can be applied to the data.

Model differences resulting from variations in minor waveform detail are not strongly supported by the data. Because the middle passband of the seismograms is corrupted by microseismic noise, we had to use a large smooth weighting factor of $\sigma = 0.1$–0.3, which caused model details to be smoothed. This means that the inversion, and thus the final structure obtained, was dominated by the P_s converted phase (Fig. 6). Minor model differences may therefore result from noise but they may also indicate small-scale local and shallow structural heterogeneities.

The primary structural characteristics described above are fairly consistent, however. Stations HOT06 and HOT07 consistently show structures of the first type from all backazimuths. Structures obtained for stations HOT08 and HOT09 are hybrids of the first and second types. For station HOT08, a structure of the first type is obtained for earthquakes arriving from the north, the second type for earthquakes from the northeast, and a hybrid type, with high velocity gradients at shallow depths but little variation in velocity gradient below

this, for earthquakes from the southwest. Station HOT09 is characterized mostly by structures of the first type, although, in the structure obtained using earthquakes from the north backazimuth, the deep interval with enhanced velocity gradients is poorly developed. Structures beneath station HOT10 are hybrid or of the second type.

There is some spatial and geological coherence in the pattern shown. Stations HOT06 and HOT07, both in the southeast of the area, consistently show structures of the first type. Stations HOT08 and HOT09 lie in the northwest of the area and show dominantly structures of the second type or hybrid structures. The rocks in the study area age to the northwest (Fig. 1). Stations HOT06 and HOT07 lie on the 10.5–11.5 Ma isochron, station HOT10 lies close to the 13 Ma isochron, and stations HOT08 and HOT09 lie close to the 15 Ma isochron. It thus appears that structures with the clear tripartite character of the first type are better developed in younger, landward areas than in older, seaward areas.

All of the main features observed in earlier refraction studies are confirmed in those of our models that display structures of the first type. The very high velocity gradient at shallow depth, and the sharp contrast with the region of very low velocity gradients below, was first noted by Flovenz (1980). He found the gradients in the shallow layers to be $\sim 0.6\ s^{-1}$ and termed this the 'upper crust'. This figure compares well with our estimates of gradients of up to about $\sim 0.8\ s^{-1}$. The region of almost constant velocity below the 'upper crust' was termed by Flovenz (1980) the 'lower crust'. The velocities we observe at the bottom of this interval are in good agreement with the refraction results of Darbyshire *et al.* (1998) and Menke *et al.* (1998).

Below the region of almost constant velocity, there is an abrupt return of relatively high velocity gradients, starting typically at depths of 23–27 km. This probably corresponds to the deep reflector observed in recent, long refraction profiles, associated with an increase of *P*-wave velocity from about 7.1 to 7.7–7.8 km s^{-1}, and has been termed the 'Moho' (e.g. Bjarnason 1993; White *et al.* 1996; Staples *et al.* 1997; Darbyshire *et al.* 1998; Menke *et al.* 1998). The nature of this 'Moho' remains poorly understood from the refraction data, however. Although Bjarnason (1993) reported a refracted arrival with an apparent velocity of 7.7 km s^{-1}, which was interpreted as P_n, very few mantle diving ray arrivals have been reported from other refraction studies. Our data suggest a region of enhanced velocity gradients throughout a depth range of about 2–4 km below most parts of the area. The clarity of this feature is variable, however, and in some places it is weak or essentially absent.

Some shallow structural details are also worthy of mention. The northwest fjords of Iceland contain a number of old, eroded central volcanoes and rift zones (Kristjansson & Johannesson 1996; Johannesson & Saemundsson 1998). These features are expected to be associated with relatively high seismic velocities at shallow depth. An extinct volcano lies approximately 10 km southwest of station HOT09 (Fig. 1), and exceptionally high velocities are indeed seen in the structure obtained from that backazimuth at 5–10 km depth (Fig. 14). Similarly, there is an extinct volcano approximately 7 km northeast of station HOT07, and relatively high velocities are detected at 5–10 km depth in the structure from that backazimuth (Fig. 15). The only other profile in which such a feature is seen is that for station HOT08 from the southwest backazimuth (Fig. 14), which is an area that lies out to sea. The other stations do not lie within a distance of 20 km of known extinct volcanoes. The method returns an average structure for a volume of crust that may extend out to about 10 km from the station at mid-crustal levels and up to 20 km at depths of 30–40 km, at the base of the crust. (For receiver functions with a dominant period of 3–5 s, corresponding to a wavelength ~ 14 km, the radius of the first Fresnel zone is ~ 20 km.)

The depths at which velocities rise to 3.7 and 4.1 km s^{-1} are shown in Fig. 18. These correspond approximately to the bases of the upper and lower crust respectively. The thicknesses of the layers near to the bases of the upper and lower crust are 1 and 2 km respectively. Since the upper crust is highly laterally heterogeneous, the depth to its base varies considerably with backazimuth at a single station. Such depth variations for the base of the lower crust are small, and only amount to the thickness of a single layer used in the inversion. Station HOT08 gives the most backazimuthal variation, which amounts to ± 2.5 km at the base of the upper crust, and ± 2 km at the base of the lower crust. Although there are very few data, there is a general tendency for the base of the upper crust to shallow

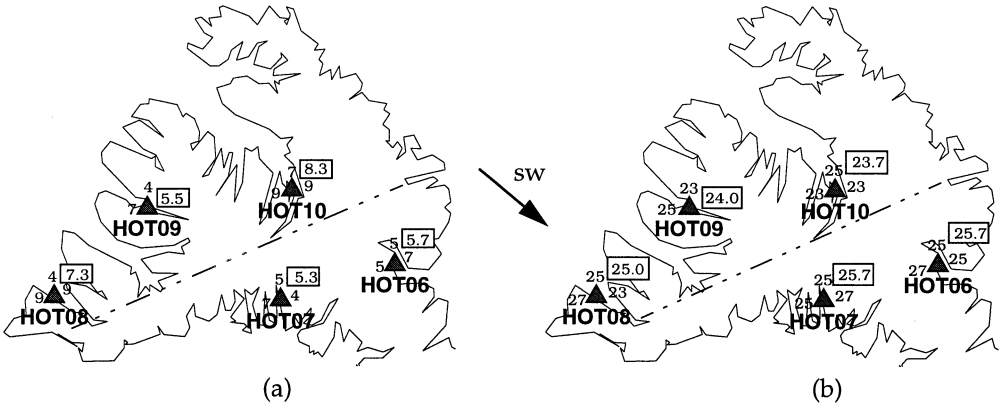

Figure 18. Depths at which velocities obtained from the joint inversions rise above 3.7 km s^{-1} and 4.1 km s^{-1}, which are the average velocities found for the bases of the upper and lower crusts from refraction data throughout Iceland. Single digits: depths obtained from inverting the data from the three backazimuths. The positions of the digits around the stations indicate the backazimuths of the earthquakes used. Numbers in boxes: depths averaged over the three backazimuths (two for station HOT09). (a) The base of the upper crust, (b) the base of the lower crust.

towards the southeast (Fig. 18a). This is in agreement with the predictions of surface geology, which is dominated by lava layers that dip towards the southeast. Surface lavas dip towards the rift zone from whence they originated because progressive subsidence beneath their own weight is greatest there, where they are thickest (Palmason 1980). The base of the upper crust is thought to shallow beneath rift zones, i.e. to shallow in the down-dip direction, and this is the tendency shown in our results. The base of the lower crust deepens in the down-dip direction (Fig. 18b).

Taken overall, our results suggest that there is considerable lateral variation in fundamental seismic structure beneath the northwest fjords of Iceland. This is not a surprising result. Iceland is highly laterally heterogeneous. At shallow depths it is constructed of a mixture of emplaced vertical, planar dykes, 3-D intrusions, horizontal lava flows and hyaloclastite formations, all of which have their sources at linear spreading centres, most of which contain one or more circular central volcanoes. The rising of melt to feed shallow vulcanism, possibly in diapiric form and possibly along linear zones, will ensure that this extreme lateral heterogeneity extends to deeper levels also. In such an environment it would be surprising if one type of seismic structure were laterally ubiquitous.

ACKNOWLEDGMENTS

This research was funded by the Natural Environment Research Council (NERC) grants GST/02/1238 and GR3/10727. The data used were collected as part of the Iceland Hotspot Project, other participants of which were Richard Allen, Bergur H. Bergsson, Palmi Erlendsson, Steinunn Jakobsdottir, Bruce Julian, W. Jason Morgan, Guust Nolet, Matthew Pritchard, Sturla Ragnarsson, Ragnar Stefansson and Kristin Vogfjord. We thank the NSF (grant EAR 9417918) and the IRIS/PASSCAL instrument center for technical assistance in deploying and running the seismic network. We acknowledge Bruce. R. Julian and W. Menke for useful discussions. We also thank two anonymous reviewers whose careful and detailed reviews greatly improved the manuscript.

REFERENCES

Ammon, G.J., Randall, G.E. & Zandt, G., 1990. On the nonuniqueness of receiver functions, *J. geophys. Res.,* **95,** 15 303–15 318.

Bath, M., 1960. Crustal structure of Iceland, *J. geophys. Res.,* **65,** 1793–1798.

Berteussen, K.A., 1977. Moho depth determinations based on spectral ratio analysis of NORSAR long-period P waves, *Phys. Earth planet. Inter.,* **31,** 313–326.

Bjarnason, I.Th., Menke, W., Flovenz, O.G. & Caress, D., 1993. Tomographic image of the Mid-Atlantic plate boundary in Southwestern Iceland, *J. geophys. Res.,* **98,** 6607–6622.

Cassidy, J.F., 1992. Numerical experiments in broadband receiver function analysis, *Bull. seism. Soc. Am.,* **82,** 1453–1474.

Constable, S.C., Parker, R.L. & Constable, C.G., 1987. Occam's inversion: A practical algorithm for generating smooth models from electromagnetic sounding data, *Geophysics,* **52,** 289–300.

Darbyshire, F.A., Bjarnason, I.Th., White, R.S. & Flovenz, O.G., 1998. Crustal structure above the Iceland mantle plume imaged by the ICEMELT refraction profile, *Geophys. J. Int.,* **135,** 1131–1149.

Du, Z.J., Michelini, A., Panza, G.F. & Urban, L., 1998. P-SV multimode summation differential seismograms for layered structures, *Geophys. J. Int.,* **134,** 747–756.

Flovenz, O.G., 1980. Seismic structure of the Icelandic crust above layer three and the relation between body wave velocity and the alteration of the basaltic crust, *J. Geophys.,* **47,** 211–220.

Flovenz, O.G., 1992. Structure of the crust and upper mantle under Iceland according to geophysical measurements, in *Physics in Iceland* No. 6, pp. 89–104, Physics Society of Iceland, Reykjavik.

Flovenz, O.G. & Gunnarsson, K., 1991. Seismic crustal structure in Iceland and surrounding area, *Tectonophysics,* **189,** 1–17.

Gebrande, U., Miller, H. & Einarsson, P., 1980. Seismic structure of Iceland along the RRISP profile 1, *J. Geophys.,* **47,** 239–249.

Johannesson, H. & Saemundsson, K., 1998. *Geological map of Iceland, 1 : 500 000, Tectonics,* 1st edn, Icelandic Institute of Natural History, Reykjavik.

Kibblewhite, A.C., 1988. Ocean noise spectrum below 10 Hz-mechanisms and measurements, in *Natural Mechanisms of Surface-Generated Ambient Noise in the Ocean,* pp. 337–359, ed. Kerman, B., Plenum, New York.

Kibblewhite, A.C. & Wu, C.Y., 1989a. The generation of infrasonic ambient noise in the ocean by nonlinear interactions of ocean surface waves, *J. acoust, Soc. Am.,* **85,** 1935–1945.

Kibblewhite, A.C. & Wu, C.Y., 1989b. A reexamination of the role of wave-wave interactions in ocean noise generation, *J. acoust, Soc. Am.,* **85,** 1946–1957.

Kristjansson, L. & Johannesson, H., 1996. Stratigraphy and palaeomagnetism of the lava pile south of Isafjardardjup, NW-Iceland, *JOKULL,* **44,** 3–15.

Langston, C.A., 1979. Structure under Mount Rainier, Washington, inferred from teleseismic body waves, *J. geophys. Res.,* **84,** 4749–4762.

Levshin, A.L., Ratnikova, L. & Berger, J., 1992. Peculiarities of surface-wave propagation across central Eurasia, *Bull. seism. Soc. Am.,* **82,** 2464–2493.

Lomax, A., Snieder, R., 1995. The contrast in upper mantle shear-wave velocity between the East European platform and tectonic Europe obtained with genetic algorithm inversion of Rayleigh-wave group dispersion, *Geophys. J. Int.,* **123,** 169–182.

Menke, W., Brandsdottir, B., Einarsson, P. & Bjarnason, I.Th., 1996. Reinterpretation of the RRISP-77 Iceland shear-wave profiles, *Geophys. J. Int.,* **126,** 166–172.

Menke, W., West, M., Brandsdottir, B. & Sparks, D., 1998. Compressional and shear velocity structure of the lithosphere in northern Iceland, *Bull. seism. Soc. Am.,* **88,** 1561–1571.

Ozalaybey, S., Savage, M.K., Sheehan, A.F., Louie, J.N. & Brune, J.N., 1997. Shear-wave velocity structure in the northern basin and range province from the combined analysis of receiver functions and surface waves, *Bull. seism. Soc. Am.,* **87,** 183–199.

Palmason, G., 1971. *Crustal Structure of Iceland from Explosion Seismology,* Soc. Sci. Isl., Prentsmidjan Leiftur, Reykjavik.

Palmason, G., 1980. A continuum model of crustal generation in Iceland; kinematic aspect, *J. Geophys.,* **47,** 7–18.

Saemundsson, K., 1979. Outline of the geology of Iceland, *Jokull,* **29,** 7–28.

Staples, R.K., White, R.S., Brandsdottir, B., Menke, W., Maguire, P.K.H. & McBride, J.H., 1997. Faeroe–Iceland Ridge experiment 1. Crustal structure of northeastern Iceland, *J. geophys. Res.,* **102,** 7849–7866.

White, R.S., McBride, J.H., Maguire, P.K.H., Brandsdottir, B., Menke, W., Minshull, T.A., Richardson, K.R., Smallwood, J.R., Staples, R.K. & the FIRE Working Group, 1996. Seismic images of crust beneath Iceland contribute to long-standing debate, *EOS, Trans. Am. geophys. Un.,* **77,** 199–200.